Soft Matter

Slip of soft permeable particles near a wall

Journal:	*Soft Matter*
Manuscript ID	SM-ART-02-2021-000242.R1
Article Type:	Paper
Date Submitted by the Author:	20-Mar-2021
Complete List of Authors:	Zakhari, Monica; The University of Texas at Austin, Department of Chemical Engineering and Texas Materials Institute Bonnecaze, Roger; The University of Texas at Austin, Department of Chemical Engineering and Texas Materials Institute

Soft Matter

ARTICLE TYPE

Cite this: DOI: 00.0000/xxxxxxxxxx

Slip of soft permeable particles near a wall

Monica E. A. Zakhari[a] and Roger T. Bonnecaze*[a]

Received Date
Accepted Date

DOI: 00.0000/xxxxxxxxxx

The slip and stick of soft permeable particles sliding near a smooth surface is determined by computing flow, pressure and shape of a particle pressed against a surface due to the osmotic pressure of the surrounding suspension and its translation at constant velocity parallel to the surface. We present a poro-elastohydrodynamic lubrication theory that accounts for the interplay of the viscous pressure force on the elastic deformation of the particle and the flow through the particle pores. At high particle velocities, the particles move along an elastohydrodynamic film of fluid causing the particles to slip on the surface. For finite particle permeability, there is a critical particle velocity determined by the permeability relative to the thickness of the film and a ratio of the viscous and elastic forces that cause a portion of the particle to contact the surface and stick. In this case the magnitude of pressure in the lubricated film is lower compared to their impermeable counterpart sliding against a smooth surface at the same speed. The particle pores offer an alternative route for the fluid in the film, reducing the lubrication pressure resulting in the particle contacting the surface. A universal function is deduced to predict this transition for a range of poro-elastohydodynamic interactions. The drag force of the particle sliding along the surface up to the contact is also determined and found to follow a universal function. These results demonstrate the possibility of dynamic stick-slip transitions via control of particle properties instead of wall surface treatments.

1 Introduction

Complex fluids are materials that are sophisticated in their complexity on a multitude of length scales. Colloidal systems are exceptionally attractive from fundamental, industrial, and technological perspectives. The ability to tailor macroscopic behavior of colloidal suspensions by tuning the individual particle properties makes colloidal systems ubiquitous for several industrial applications, such as in functional coatings[1–3], pharmaceuticals[4,5], and foods[6–8]. Exploiting these materials in industrial applications necessitate processing them in confined spaces, such as by extrusion and 3D printing[9], which makes them susceptible to wall slip near smooth surfaces. The behavior of concentrated colloidal suspensions is strongly affected by their interaction with the bounding surfaces.

The presence of slip hampers accurate characterization of rheological behavior of these materials. Slip originates from a lack of adhesion between the sheared particle-suspension and bounding surfaces. The presence of slip results in a thin layer of fluid that is depleted from the suspended particles, which results in non-uniform macroscopic properties. Slip alters the resulting flow field and leads to errors in macroscopic flow measurements such as relations between shear stress and shear rate, especially the yield stress[10–12]. In the absence of slip, i.e. under no-slip conditions, the flow of concentrated suspensions of soft particles is characterized by a yield stress σ_y, while when slip is present, the material exhibits an apparent yield stress $\sigma_y^s (< \sigma_y)$, also known as slip yield stress below which particle tend to stick to the wall[12]. Slip-stick in concentrated colloidal suspensions and the resulting flow gradient discontinuity has significant implications and is unavoidable during processing of these materials. Boundary effects can also lead to the development of flow instabilities similar to those developed in extruded polymer melts, such as secondary-flow instabilities[13] and melt fracture[14–16].

Slip is often desirable in applications where transport efficiency is crucial, inspired by many biological and natural processes. Slip is essential for the transport of foods throughout the digestive tract[17], the motion of red blood cells through microvascular networks to deliver oxygen and nutrients[18], and intracellular flows in large plant cells, i.e. cytoplasmic streaming, for fast and efficient transport of nutrients and other chemicals within the cell[19]. Furthermore, mucus acts as biological lubricant for organs such as the eye; it protects the eye by allowing slip to rapidly expel foreign particles[20]. The efficient transport promoted by slip as observed in several biological systems can also be exploited in industrial applications, such as microfluidic devices[21,22], sewage treatment[23], oil extraction[24], and food processing[25,26]. All of these applications require control over slip-stick transitions, which can be achieved by regulating bounding surface properties.

[a] McKetta Department of Chemical Engineering, The University of Texas at Austin, Austin, Texas 78712, USA.
* E-mail: rtb@che.utexas.edu

Wall-slip can be suppressed by manipulating wall surface, physically and/or chemically. Physical implementation of surface asperities, i.e. roughening the wall surface, can disrupt the thin lubricated layer and suppress slip. Rough surfaces have been achieved by sandblasting[27,28], machining[29,30], creating surface features by serrated tools for example[31]. The effect of roughness degree on the slip behavior is examined in detail in[32,33]. Inhibiting slip by surface roughness requires creating surface features that are much larger that the particle size or the largest dominating heterogeneity. This criterion is the reason why it is difficult to suppress slip by surface roughness in colloidal gels, in which case aggregates coarsen as the gel ages[34]. While surface roughness is often successful to prevent slip, an increased surface roughness has been found to result in fracture[32]. Seth *et al.* (2008)[35] proposed controlling slip-stick behavior via chemical modifications of the surface. The idea originates from the observation that lubricating films are often on the order of $2-10$ nm[11,28]. Over this short length scale, short-range interactions between particle and wall become more relevant. Attractive forces originate from van der Waals interactions with the wall or more generally the hydrophobic nature of the surface, which result in sticking behavior rather than slip. Repulsive forces are a consequence of hydrophilic surfaces and this leads to slip of particles when sheared against it[12,35,36]. In general, it is demonstrated that slip can be effectively suppressed by the physical and/or chemical surface treatment, controlling the degree of slip-stick is more challenging using this approach[37].

In this paper, we propose controlling the slip-stick behavior by tuning particle properties rather than wall surface properties. Recent studies suggest that surface features of soft impermeable particle strongly influence its adhesion to a rigid wall when sliding against it[38]. However, the interrelationship between particle internal structure and confinement effects remains an unexplored territory[39]. Based on their architecture, soft permeable particles can be broadly classified as microgels and star polymers[39]. The softness and deformability of these particles are well-regulated by the degree of crosslink density and the number of arms for microgels and star polymers, respectively[39,40]. When compressed, soft particles are able conform in shape and size by expelling solvent from their interior. The conformability of soft particles is a direct consequence of their internal structure. An effective description of the particle internal structure for different particle architecture remains an experimental challenge[39]. However, numerical simulations can have a unique contribution, where the effect of the particle internal structure can be incorporated by an effective permeability[41,42]. The particle permeability effectively regulates the flow through the particle pores. Here, we extend the non-contact elastohydrodynamic lubrication theory initially presented in[11,28], and modified later to account for short-range interactions with the wall in[35]. This theory explains the slip behavior in soft *impermeable* particles by coupling the elastic deformation of the particle due to bulk osmotic pressure and gap hydrodynamics. With the aim of investigating the slip behavior of soft *permeable* particle suspensions, we derive a model that accounts for fluid flow through the particle pore as it slides near the wall. The presented model is then used to examine the interplay between particle internal structure, i.e. its permeability, and its slip-stick behavior near a wall.

The remainder of this paper is organized as follows. The microscopic theory for slip of permeable particles near the wall – the poro-elastohydrodynamic theory – is presented in both dimensional and dimensionless forms in Sec. 2. In Sec. 2, we also present the model parameters used in the numerical simulations. This is followed by a description of the numerical procedure used to solve the resulting set of equations in Sec. 3. The obtained numerical results are presented in Sec. 4. Finally, the paper is concluded with a discussion in Sec. 5.

2 Microstructural theory for slip in permeable particle suspensions

In this section, we present an extension of elastohydrodynamic lubrication theory that accounts for the poroelastic nature of the particles, which originates from their permeable structure. Soft permeable particle such as microgels, star-polymers, and supramolecular particles can be modeled as poroelastic particles with permeability κ.

Consider a concentrated suspension of randomly-arranged soft poroelastic particles moving parallel to a smooth rigid wall due to a shear or pressure-driven flow. The suspension volume fraction, ϕ, is higher than random close packing fraction of hard-sphere systems, i.e. $\phi > 0.64$. At such high densities, particles are trapped in tight cages by their neighboring particles and the wall, on the one hand. Therefore, particle displacements relative to other particles and particle migration are neglected. On the other hand, particles are compressed and deformed on all sides by particle-particle contacts and a particle-wall contact. The wall is assumed to be perfectly rigid, since it has a much higher modulus than the soft particles considered here. A particle near the wall is compressed against the rigid wall due to the surrounding particles. Particles near the wall can hence be assumed to only translate and not rotate or migrate due the confinement of the surrounding particles. When the particle is at rest, Hertzian contact pressure acts on the particle and a facet develops. When the particle is moving, a lubricating film is formed and the fluid pressure in the gap creates the facet. In this case, the pressure field is not axisymmetric and so the facet is no circular. The suspension moves with some velocity distribution that varies normal to the wall and the particles near the wall can move at a finite velocity due to the elastohydrodynamic lubrication of the particle-wall contact. The particle experiences non-contact elastohydrodynamic lift and drag forces, F_L and F_D, due to interactions with the wall.

Specifically, let us consider the behavior of single particle of radius R pressed against the smooth wall by the bulk osmotic pressure of the suspension. The particle translates horizontally at a constant applied sliding speed U as depicted in Fig. 1. Assuming no bulk rearrangements, the particle will remain locked in its place relative to the wall by its neighbors with an overlap with the wall of $h_0+\delta$. This deformation results in a facet of radius r_0.

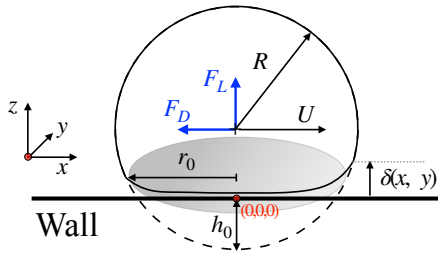

Fig. 1 Schematic of a soft particle of radius, R, compressed against a smooth rigid wall and sliding against it with a velocity U. The particle forms a contact facet of radius $r_0 = \sqrt{Rh_0}$ at rest, where h_0 is the initial compression of the particle. The deformed particle surface is denoted by $\delta(x,y)$. The particle experiences non-contact elastohydrodynamic lift and drag forces, F_L and F_D, due to interactions with the wall. The origin of the Cartesian coordinate system is fixed at the wall below the center of the particle.

2.1 Theory of poro-elastohydrodynamic slip

The present model extends the elastohydrodynamic theory presented by Meeker and co-workers [11,28] for impermeable soft particles to a porous, permeable soft particles. The original model couples Reynolds lubrication equation [43] in the gap with the general integral equation for contact mechanics [44]. This earlier model was later modified to account for short-range attraction and repulsion with the wall [35]. Here, we extend the original model by allowing flow through the internal structure of the porous particle through an additional coupling via Darcy's law [45]. The resulting governing equations, which describe the long-time, steady-state behavior are

$$\nabla \cdot \left(\delta^3 \nabla p\right) = -6\eta_s U \partial_x \delta + 12\eta_s \upsilon(x,y), \tag{1a}$$

$$\delta(x,y) = -h_0 + \frac{x^2+y^2}{2R} + u_z(x,y)|_{z=0}, \tag{1b}$$

$$u_z(x,y)|_{z=0} = \frac{1-\nu^2}{\pi E} \int_{-\infty}^{\infty}\int_{-\infty}^{\infty} \frac{p(\xi,\theta)}{\left((x-\xi)^2+(y-\theta)^2\right)^{\frac{1}{2}}} d\xi d\theta, \tag{1c}$$

where p is the hydrodynamic pressure in the gap between the particle and the wall, and it is measured with respect to the far-field fluid pressure away from the wall. In Eq. 1a, η_s is the solvent viscosity, U is the particle velocity as shown in Fig. 1. The operator ∇ is the derivative taken over the two-dimensional Cartesian coordinates (x,y), where the origin is located at the wall and beneath the center of the particle. Equation 1a is coupled with the gap height, which is given by Eq. 1b. Equation 1b described the particle profile as the summation of the undeformed particle shape approximated by a parabola, $-h_0 + \left(x^2+y^2\right)/2R$, and the particle elastic deformation $u_z(x,y)|_{z=0}$ [46]. This elastic deformation depends on the hydrodynamic pressure in the gap acting on the particle, and this relation is described by Eq. 1c. Equation 1c describes the long-time solution of Hertz contact problem for a poroelastic particle approaching a semi-infinite plane [44,47]. In Eq. 1c, E is the particle modulus, ν is Poisson's ratio, and (ξ,θ) are the integration variables in Cartesian coordinates. Finally, the vertical fluid velocity in the gap, υ, describes the velocity by which the fluid enters the particle pores near the wall, and hence defines the net fluid flow from/to the particle. At steady state the rate of deformation of the elastic structure vanishes and does not influence the flow in the porous particle.

Since we only investigate the steady state slip behavior of permeable particles, flow from/to the particle is governed by Darcy's law [45,48]. From the particle perspective, the amount of fluid flowing from/to the particle must be conserved. In order to calculate the vertical fluid velocity in the gap υ and satisfy mass conservation for the fluid and Darcy's law, we seek solutions of the Laplace equation for the pressure which is valid throughout the entire particle Ω,

$$\nabla^2 p = 0 \text{ for } (x,y,z) \in \Omega. \tag{2}$$

It is to be noted that, according to the lubrication theory [43], the pressure in the gap is constant in the z-direction, leading to vanishing vertical fluid velocity in the gap, however the pressure is not constant inside the particle. The mutual coupling of lubrication theory, Darcy's law, and particle elastic deformation is the origin of the vertical fluid velocity at the particle surface.

In order to calculate the vertical fluid velocity υ, only the pressure gradient at the surface of the particle is required. In this case, a boundary integral representation [49,50] of Eq. 2 is convenient, where the particle is approximated by a semi-infinite domain. A fundamental solution of the Laplace equation at a point $\boldsymbol{x}$ in three-dimensions is given by $p(\boldsymbol{x})^* \sim \frac{1}{4\pi r}$, where $r = \|\boldsymbol{x}-\boldsymbol{y}\|$ and $\boldsymbol{y} \in \Omega$ [51]. This solution satisfies the Laplace equation everywhere in the domain Ω except at the singularity location at $\boldsymbol{x} = \boldsymbol{y}$. Using this solution, the boundary value problem described by Eq. 2 can be cast in a boundary integral formulation, that is suitable for Boundary Element Method (BEM) [49–51], as

$$p(\boldsymbol{x}) = \frac{1}{4\pi}\int_{\partial\Omega}\left[p(\boldsymbol{y})\partial_{\boldsymbol{y}}\frac{1}{r} - \partial_{\boldsymbol{y}}p(\boldsymbol{y})\frac{1}{r}\right]\cdot \boldsymbol{n} dS \quad \boldsymbol{x} \in \Omega \tag{3}$$

where $\partial_{\boldsymbol{y}}\frac{1}{r} = -(\boldsymbol{y}-\boldsymbol{x})/r^3$. In the derivation of Equation 3, Green's second identity is used.

Finally, once the pressure field at the surface of the particle is obtained, the vertical fluid velocity can be calculated according to Darcy's law as

$$\upsilon = -\frac{\eta_s}{\kappa}\nabla p \cdot \boldsymbol{e}_z \text{ for } (x,y,z) \in \Omega, \tag{4}$$

where κ is the particle permeability and $\boldsymbol{e}_z$ is the unit vector in the z-direction.

2.2 Dimensionless form of the governing equations

Equations (1a-1c) are non-dimensionalized as follows. Dimensionless or rescaled variables are denoted by their corresponding capital letters. Length scales in the plane of the wall, x and y, and derivatives thereof are scaled by the contact radius r_0 (see Fig.

1), as

$$X = \frac{x}{r_0},\ Y = \frac{y}{r_0},$$

$$\frac{\partial}{\partial x} = \frac{1}{r_0}\frac{\partial}{\partial X},\ \frac{\partial}{\partial y} = \frac{1}{r_0}\frac{\partial}{\partial Y}.$$

The contact radius is the radius of the flattened surface parallel to the wall at rest, $r_0 = \sqrt{Rh_0}$[44]. Length scales normal to the plane of the wall, such as the gap height and the particle deformation in the z-direction are scaled with the initial deformation, h_0, that is

$$H = \frac{h}{h_0},\ U_Z = \frac{u_z}{h_0}.$$

Applying these scaling to the governing equations, the following non-dimensional forms are obtained

$$\nabla\cdot\left(H^3\nabla P\right) = -\partial_x H + V, \tag{5a}$$

$$H(X,Y) = -1 + \frac{X^2+Y^2}{2} + U_Z(X,Y)|_{Z=0}, \tag{5b}$$

$$U_Z(X,Y)|_{Z=0} = \lambda\int_{-\infty}^{\infty}\int_{-\infty}^{\infty}\frac{P(\Xi,\Theta)}{\left((X-\Xi)^2+(Y-\Theta)^2\right)^{\frac{1}{2}}}d\Xi d\Theta \tag{5c}$$

Far from the wall, the hydrodynamic pressure is given by the analytical expression of a rigid particle moving parallel to a smooth wall[52] as

$$P|_{X\to\infty,Y\to\infty} = \frac{X}{5H^2}, \tag{5d}$$

In Eqs. 5, the flow parameter λ is defined as $\lambda = 6\eta_s UR/\left(G_p h_0^2\right)$, where $G_p = \pi E/\left(1-\nu^2\right)$. The boundary integral Eq. 3 becomes

$$P(\boldsymbol{X}) = \frac{1}{4\pi}\int_{\partial\Omega}\left[P(\boldsymbol{Y})\partial_{\boldsymbol{Y}}\frac{1}{\bar{r}} - \partial_{\boldsymbol{Y}}P(\boldsymbol{Y})\frac{1}{\bar{r}}\right]\cdot\boldsymbol{n}d\bar{S} \quad \boldsymbol{X}\in\Omega \tag{6a}$$

where $\partial_{\boldsymbol{Y}}\frac{1}{\bar{r}} = -\left(\boldsymbol{Y}-\boldsymbol{X}\right)/\bar{r}^3$, $\bar{r} = \|\boldsymbol{X}-\boldsymbol{Y}\|$, and $d\bar{S} = r_0^2 dS$. The dimensionless vertical fluid velocity is given by,

$$V = -\frac{12\kappa R^{1/2}}{h_0^{5/2}}\,\partial_{\boldsymbol{Y}}P\cdot\boldsymbol{e}_z. \tag{6b}$$

It is to be noted that the pressure at the particle surface denoted by $\partial\Omega$ is equal to the hydrodynamic in the gap from Eqs. 5, which is independent of the gap height as dictated by the lubrication theory[43];

$$P|_{\boldsymbol{X}\in\partial\Omega} = P(X,Y) \tag{6c}$$

In Eqs. 5 and 6, the pressure is scaled with the characteristic hydrodynamic pressure in the gap P_c is given by

$$P_c = \frac{6\eta_s UR^{1/2}}{h_0^{3/2}}, \tag{7}$$

and the vertical fluid velocity, $V = v/V_c$, is scaled with the characteristic velocity

$$V_c = \frac{Uh_0^{1/2}}{2R^{1/2}}. \tag{8}$$

2.3 Dimensionless groups specification

To proceed with simulations, realistic estimates of particle and fluid properties are to be specified. Simulations are fully described in terms of the flow parameter λ, and the dimensionless permeability $\bar{\kappa} = \kappa/h_0^2$. A summary of the simulation parameters is given in Table 1. Representative values for a microgel particles are used to obtain the results in Sec. 4. In the absence of flow, the effect of system density and the resulting osmotic pressure acting on the particle is expressed by the initial overlap, h_0, and the initial contact radius, r_0. The particle compression ratio, $\zeta_0 = h_0/R$, is related to the volume fraction of the system as[53]

$$\zeta_0 = 1 - \left(\frac{\phi_{\mathrm{RCP}}}{\phi}\right)^{\frac{1}{3}}, \quad \text{for}\phi > \phi_{\mathrm{RCP}}, \tag{9}$$

where $\phi_{\mathrm{RCP}} = 0.64$ is the volume fraction at random close packing. Similar properties to those used in[11,35] are employed in the present study. Microgel particles of $R = 220$nm and an initial overlap $h_0 = 22$nm, which corresponds to a overall system volume fraction of $\phi \approx 88\%$. The particle is suspended in water, $\eta_s = 1$ mPa $\cdot$ s. The mechanical properties of these particles are described by $G_p \sim 10^5$Pa. Estimates of particle permeability available in literature are limited. The permeability of microgels also depend on polymer concentration, cross-link density, and the permeating fluid velocity[54]. However, one can estimate the pore-size and permeability based on the particle size. It is reasonable to assume that the pore-size l_{pore} is at least a couple of orders of magnitude lower than the particle size, i.e. $l_{\mathrm{pore}} \sim 0.01R$. The permeability is proportional to square of the pore size $\kappa \sim l_{\mathrm{pore}}^2$, hence the permeability can be estimated as $\kappa \sim 10^{-18}\mathrm{m}^2$.

Table 1 Model parameters and range of values.

Parameter	Symbol	Physical Value
Solvent viscosity	η_s	1 mPa $\cdot$ s
Particle modulus	G_p	10^5 Pa
Particle radius	R	220 nm
Initial overlap	h_0	22 nm
Flow parameter	λ	$[0.0001-5]$
Dimensionless permeability	$\bar{\kappa}$	$\{0, 0.207, 1.03, 2.07, 4.13\}\times 10^{-3}$

3 Numerical solution

The numerical procedure for solving the coupled equations 5 and 6 is presented in detail in this section.

3.1 Computation of the vertical component of fluid velocity

The vertical fluid velocity at the particle surface V is required to solve Eqs. 5a-c. As explained in Sec. 2.1, Boundary Element Methods (BEM) can be used in this case as expressed in Eq. 6[49,50].

To solve Eq. 6 numerically using BEM, the surface of the par-

ticle is discretized into N_p patches. Assuming that the pressure and its gradient are constant over each patch k, Eq. 6a can be rewritten, for each patch m, as

$$A_{mk}\left(\partial_{\boldsymbol{Y}_k} P\right) = \sum_{k=1}^{Np} B_{mk} P_k. \tag{10a}$$

where

$$A_{mk} = \frac{1}{4\pi} \int_{\partial\Omega} \frac{1}{\|\boldsymbol{X}_m - \boldsymbol{Y}_k\|} \cdot \boldsymbol{n}_k d\bar{S}, \tag{10b}$$

$$B_{mk} = -\frac{1}{4\pi} \int_{\partial\Omega} \frac{\boldsymbol{Y}_k - \boldsymbol{X}_m}{\|\boldsymbol{X}_m - \boldsymbol{Y}_k\|^3} d\bar{S}. \tag{10c}$$

The solution can be obtained as follows: Given the pressure field P and the particle shape H, the midpoint coordinates and outward normal to each patch are calculated. For each patch m, the integrals A_{mk} and B_{mk} for all patches k are calculated using Gaussian 2D quadrature. Finally, we solve Eq. 6a for $\partial_{\boldsymbol{Y}_k} P$ as

$$\partial_{\boldsymbol{Y}_k} P = A^{-1}_{mk} B_{mk} P_k. \tag{11}$$

These values are used to obtain the vertical fluid velocity to the surface according to Eq. 6b.

3.2 Numerical solution of poro-elastohydrodynamic equations

Equations 5a-c are simultaneously solved for pressure P, gap height H, and particle deformation $U_Z(X,Y)|_{Z=0}$ over a planar domain (X,Y) parallel to the wall. This domain is discretized into equal-sized square elements in each direction, N_X and N_Y, respectively. This domain is chosen to be large enough, so that the particle deformation is $U_Z(X,Y)|_{Z=0} = 0$ and consequently $H = -1 + \left(X^2 + Y^2\right)/2$ at the boundaries. The boundary condition Eq. 5d is applied at the perimeter of the computational domain.

An iterative scheme is used to solve Eqs. 5. With an initial guess for the pressure P^0, Eq. 5c is solved using numerical integration scheme, namely the trapezoidal rule, for $U_Z(X,Y)|_{Z=0}$, which is used to compute the gap height H from Eq. 5b. Finite difference approximations of Eq. 5a are used to obtain an updated hydrodynamic pressure P. Convergence is reached when the norm of the difference in pressure at each point in the domain is less than 10^{-7}, or when the drag and lift force between iterations is the same up to the fifth decimal point. The drag and lift forces are calculated as

$$F_D = -\int\int P\, \partial_X H + \frac{H}{2}\partial_X P - \frac{1}{6H} dX dY, \tag{12a}$$

$$F_L = \left(\frac{R}{h_0}\right)^{\frac{1}{2}} \int\int P dX dY, \tag{12b}$$

where these forces are scaled by $6\eta R u$. Finally, to ensure smooth convergence, under-relaxation is employed for $U_Z(X,Y)|_{Z=0}$ in order to avoid unrealistically large particle displacements per iteration step, specially in the case of highly permeable particles.

4 Results

The wall-slip behavior of permeable particles is presented and compared with impermeable particles of similar properties. Simulations are performed at different sliding speeds, characterized by the flow parameter, λ, and different permeability values, described by, $\bar{\kappa}$.

4.1 Slip behavior of permeable particle

The behavior of permeable particle is discussed in comparison with that of impermeable particle of the same properties, subject to same sliding speed. Figure 2 shows the particle profile at the centerline of impermeable and permeable particles in the direction of motion. In the case of impermeable particle, the particle shows an asymmetric deformation at the centerline of the particle. Underneath the particle center the particle facet is almost uniform, while upstream the particle is protruded close to the wall. This asymmetry is in fact a result of the pressure profile in the lubricated layer of fluid between the particle and the wall. Figure 3 shows the pressure profile at the centerline of impermeable and permeable particles in the direction of motion. The pressure underneath the particle is positive everywhere except at the rear of the particle. The negative pressure underneath the protruded surface and at the rear of the particle leads to fluid being pulled in the gap. This pressure gradient created by the negative pressure maintains flow in the lubricated fluid film between the particle and the wall.

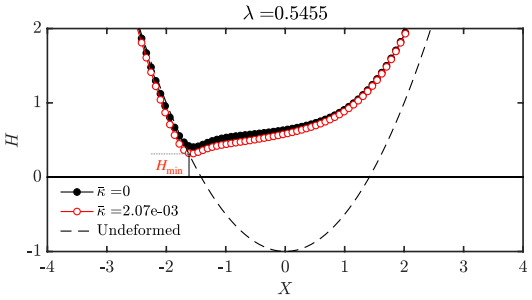

Fig. 2 The particle profile along $X-$axis – the sliding direction – of an impermeable particle (black filled symbols), i.e. $\bar{\kappa} = 0$, and permeable particle (red open symbols), $\bar{\kappa} = 2.07 \times 10^{-3}$. Both particles are sliding against the wall with a speed characterized by $\lambda = 0.5455$. The dashed line indicates the shape of the undeformed particle.

The pressure profile of a permeable particle sliding near a wall with the same speed is also plotted in Fig. 3. The overall pressure profile in the gap is lower than the pressure developed beneath the impermeable particle sliding near the wall to maintain flow in the narrow gap. The permeable particle moves closer to the wall as a result of this pressure profile. In order to understand this behavior, the flow through the particle is examined.

The vertical fluid velocity V is plotted in Fig. 4a for the case of permeable particle. It is to be noted that the vertical fluid velocity is vanishing for impermeable particles as shown by the black line in Fig. 4b. Positive values of V indicate fluid flow to the particle, while negative values denote flow from the particle. Figure 4b shows that fluid flows from inside the particle to the gap at the

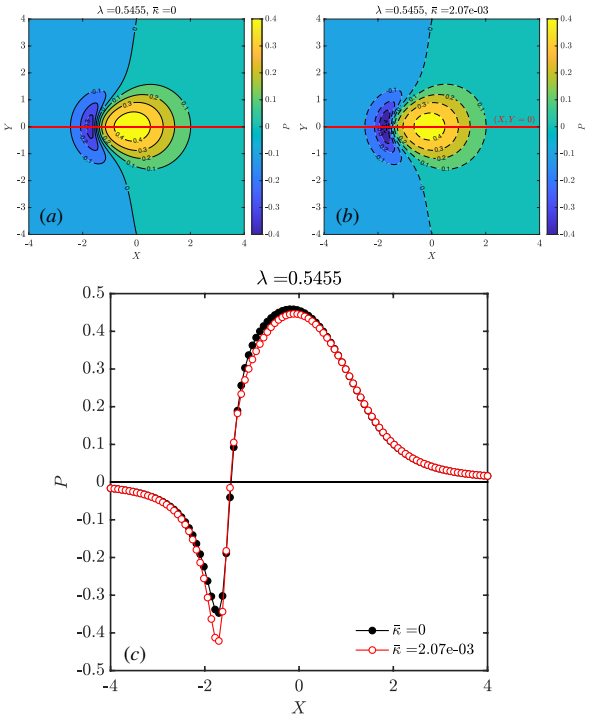

Fig. 3 Pressure contour plots (lines and bands) beneath (a) an impermeable particle, $\bar{\kappa}=0$, and (b) a permeable particle, $\bar{\kappa}=2.07\times10^{-3}$, sliding against the wall at a speed characterized by $\lambda=0.5455$. (c) Pressure profile beneath both impermeable (black filled symbols) and permeable (red open symbols) particle center-line and along the sliding direction denoted by the red lines in (a) and (b), respectively.

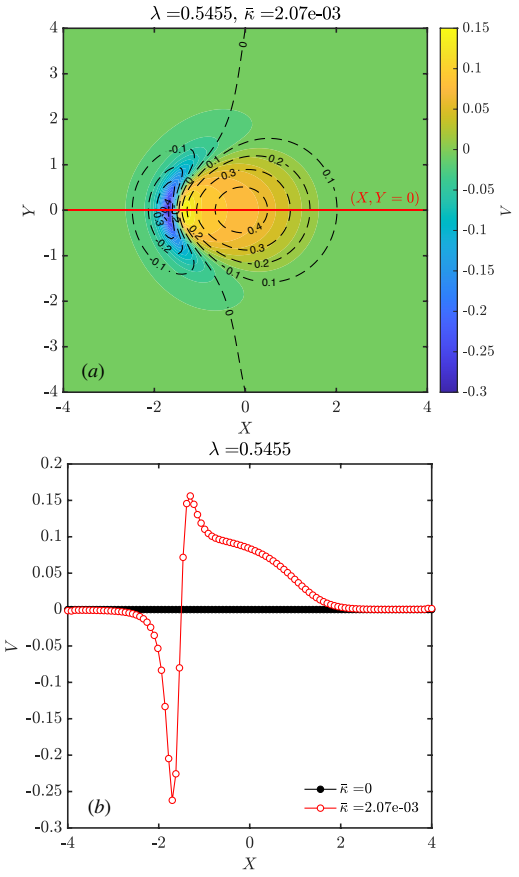

Fig. 4 (a) Pressure contour line superimposed on vertical fluid velocity contour bands beneath a permeable particle, $\bar{\kappa}=2.07\times10^{-3}$, sliding against the wall at a speed characterized by $\lambda=0.5455$. (c) Vertical fluid velocity profile beneath both impermeable (black filled symbols) and permeable (red open symbols) particle center-line and along the sliding direction denoted by the red lines in (a). Note that the vertical fluid velocity is zero for impermeable particles as shown by the black curve in (b). The net flow in the permeable particle case is calculated as $\bar{Q}=\int_S V dS=0.1295$.

rear of the particle, while fluid flows to the particle at the particle front.

A permeable particle sliding close to a wall is closer than its impermeable counterpart with the same properties and sliding at the same speed. This behavior is a result of the coupling between the fluid properties in the lubricated film and fluid flow through permeable particle. A sketch depicting the major differences in slip behavior between impermeable and permeable particles is shown in Fig. 5. When a permeable or impermeable particle slides near a wall a thin film of fluid forms at the facet between the particle and the wall. A pressure gradient forms within this film. This pressure gradient acts to maintain the lubricated layer in the gap, and this effect is explained as follows. For impermeable particles, far-field fluid is drawn *to* the negative pressure side of gap at the rear of the particle. The fluid is expelled *from* the positive pressure side of the gap at the front of the particle, see Fig. 5a. In the case of permeable particles, an additional flow contribution emerges due to the ability of the particle to draw in and expel fluid through its pores. The negative pressure at the particle rear draws fluid to the film from the far-field fluid *and from within the particle pores*. Fluid is expelled from the gap at the particle front *and to the particle pores*, see red arrows in Fig. 5b. This additional flow contribution from and to the particle pores at the negative and positive fluid pressure sides in the gap, respectively, results in the lower overall pressure compared to the case of impermeable particle sliding near the wall. As a result, slip is less pronounced in permeable than impermeable particles – permeable particles tend to stick to the wall.

4.2 Influence of sliding speed on the behavior of permeable particles near a wall

The effect of sliding speed on the sticky behavior of permeable particles is studied in detail in this section.

Figure 6a shows the particle profile at different sliding speeds. The slower the sliding speed, the closer the particle gets to the wall. This behavior is also observed for soft impermeable particles sliding against a rigid wall[35], and rigid particle sliding against a soft impermeable wall[55]. The corresponding pressure profile at the centerline beneath the particle is shown in Fig. 6b. The slower the sliding speed, the higher the magnitude of the pressure in the gap in both the negative and positive pressure regions.

The pressure profile in the gap has a direct effect on the fluid flow to and from the particle. Figure 7 shows the effect of sliding on the vertical fluid velocity and resulting net flow. The magnitude of fluid velocity to and from the particle increases as the

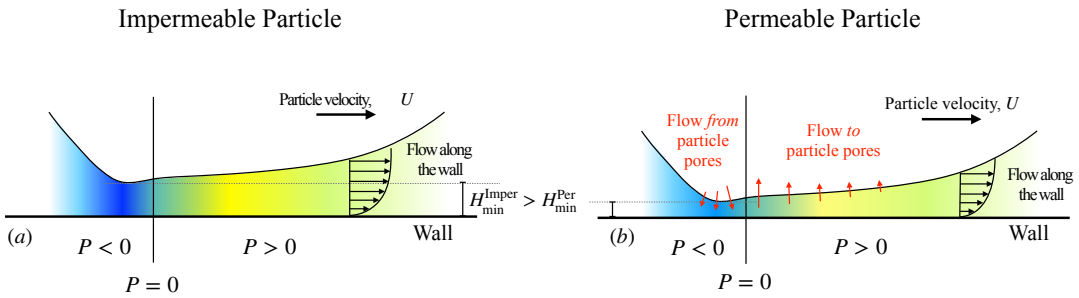

Fig. 5 Sketch of the major differences in slip behavior between (a) an impermeable and (b) a permeable particle sliding near a rigid wall. The colored sections indicate the pressure in gap. The black arrows show the flow from/to far-field fluid, while the red arrows, in the case of permeable particles in (b), show flow of from/to particle pores.

sliding speed decreases. Integrating the fluid velocity over the entire domain gives the net flow, $\bar{Q}$, through the particle. Positive $\bar{Q}$ values denote net flow to the particle and negative values denote net flow from the particle. This net flow is plotted in the inset of Fig. 7 as a function of sliding speed. The net flow is positive for all sliding speeds, i.e. the net flow is *to* the particle pores on the underside of the particle. This fluid of course leave the particle on its far side and its exit is of no consequence to the sliding near the wall. The inset in Fig 7 shows that the net flow increases as the sliding speed decreases as a result of the higher pressure magnitude at lower λ.

4.3 Influence of permeability on slip-stick behavior

In Section 4.2, we showed that the flow through the particle pores underlies the difference in slip behavior between permeable and impermeable particles sliding near a wall. In this section, the effect of permeability on the sticky behavior of permeable particles is examined. In order to efficiently study this behavior, the particle profile is characterized by the minimum height of the particle, i.e. the closest point to the wall. The net flow is plotted as a measure of the vertical fluid velocity. Finally, The pressure in the gap results in a drag force on the particle, hence it is plotted instead of the full pressure profile.

Figure 8 shows the minimum gap height, denoted by $H_{\min}$, for particles of different permeability values $\bar{\kappa}$ sliding at different speeds λ. The balance between hydrodynamic forces on the particle and resistance forces from single particle deformation and osmotic pressure from the bulk dictate the extent of particle deformation. The stronger the flow, i.e. high λ, the larger the lift force experienced by the particle, which leads to more particle deformation and higher gap heights. Figure 8 shows exactly this effect – the higher the sliding speed, λ, the larger the minimum gap height, $H_{\min}$, for both impermeable and permeable particles. For large particle velocities, the minimum gap height appears to be independent of permeability; this is not the case for low particle velocities. For these cases, i.e. low λ, the minimum gap height depends on the permeability. For impermeable particles, i.e. $\bar{\kappa} = 0$, the minimum gap height decreases with decreasing sliding speed. For permeable particles, i.e. $\bar{\kappa} \neq 0$, the minimum gap height continues to decrease with decreasing sliding speed, until a critical value, λ_s – the sticking point. Beyond this sticking point, the minimum gap height becomes negative, which indicates that the lowest surface point of the particle comes in contact with the wall. The sticking point can be defined as

$$\lambda_s = \lambda|_{\min H(X,Y)=0}, \quad \forall (X,Y). \tag{13}$$

Figure 8b shows that the minimum gap height depends on the sliding speed following a power law with exponent that is independent of the permeability value, $H_{\min} \sim (\lambda - \lambda_s)^{0.50}$. The sticking point, however, decreases with decreasing permeability, and it's vanishing for impermeable particles. The dependence of sticking point on the permeability value follows a power law of type, $\lambda_s \sim \bar{\kappa}^{0.65}$, as shown in Fig. 8b. The minimum gap height when plotted against the difference between the flow parameter and the sticking point (see Fig. 9), $\lambda - \lambda_s$ result in the collapse of the data for different permeability on a universal curve that can be fitted to a power law with these average fitting parameter shown in Fig 8b. The critical speed of the particle at the onset of sticking, U_s, is determined from the sticking flow parameter, λ_s, as

$$U_s = \frac{G_p h_0^2 \lambda_s}{6\eta_s R}. \tag{14}$$

The values of the critical speeds corresponding to the sticking points at different values permeability are shown in Table 2. In practice, the value of the critical speed defines the value below which the effect of slip on suspension rheological properties cannot be neglected [11]. The critical speed can define the operating speeds in rheological experiments, such as the cone speed in a cone-plate rheometer. In suspensions of permeable particles, the critical flow speed increases with increasing permeability, which suggests that wall effects are dominant for a wider range of flow speeds with increasing permeability.

Table 2 Critical speeds calculated as $U_s = G_p h_0^2 \lambda_s / (6\eta_s R)$ for different values of dimensionless permeability, $\bar{\kappa}$, using parameters listed in Table 1 and the values of the sticking point, λ_s, also listed in the table.

Permeability, $\bar{\kappa}$	Sticking point, λ_s	Critical flow speed, U_s
0	0	0.0 mm · s^{-1}
0.21×10^{-3}	0.047	1.7 mm · s^{-1}
1.03×10^{-3}	0.166	6.1 mm · s^{-1}
2.07×10^{-3}	0.276	10.1 mm · s^{-1}
4.13×10^{-3}	0.401	14.9 mm · s^{-1}

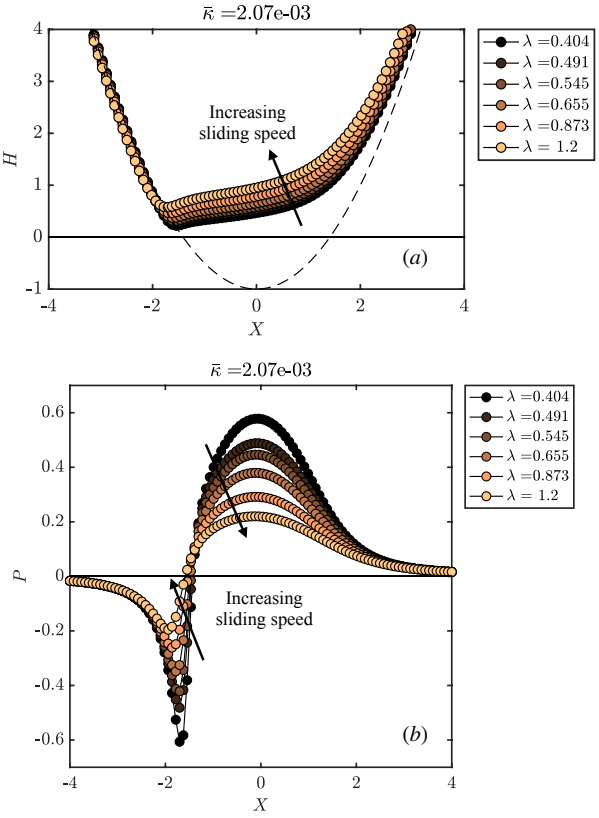

Fig. 6 Effect of the sliding speed of a permeable particle, characterized by λ, on the (a) particle profile and the (b) pressure in the gap beneath the particle, along the sliding direction, i.e. $X-$axis. Arrows indicate the direction of increasing the sliding speed.

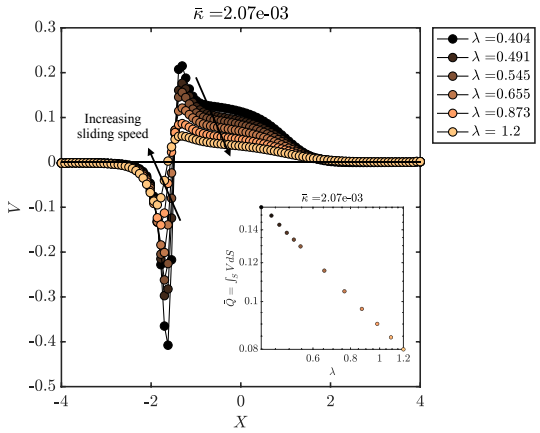

Fig. 7 Effect of the sliding speed of a permeable particle, characterized by the flow parameter λ, on the vertical fluid velocity at the particle surface plotted along the sliding direction, i.e. $X-$axis. Arrows indicate the direction of increasing the sliding speed. Inset shows the net flow to the particle as a function of the flow parameter, given by the specific discharge $\bar{Q} = \int_S V dS$.

The sticky behavior of permeable particles originates from the ability of fluid to flow through their pores. To examine this behavior and how it is influenced by the permeability, the net flow through the particle is investigated. Figure 10 shows the net fluid flow through the pores, $\bar{Q}$, of particles with different permeability values, $\bar{\kappa}$, sliding near a wall at different speeds λ. As discussed earlier in Sec. 4.2, positive $\bar{Q}$ denote flow to the particle, negative $\bar{Q}$ denote flow from the particle. Figure 10a shows that the net flow is to the particle for all values of permeability. The net flow to the particle increases with decreasing sliding speed, as shown earlier in Fig. 7. The net flow to the particle increases with increasing permeability at the same sliding speed, as shown in Fig. 10a. A universal curve can be obtained by scaling the net flow with the corresponding permeability (see Fig. 10b). The dependence of scaled net flow on the flow characteristic parameter in the gap λ obeys a power law $\bar{Q}/\bar{\kappa} \sim \lambda^{-0.80}$.

Particles sliding against the wall experience a fluid resistance force that is proportional on the fluid pressure – the drag force. Figure 11a shows the drag force, F_D, on a particle with different permeability values, $\bar{\kappa}$, sliding near a wall at different speeds λ. Figure 11a shows that the drag force increases with decreasing sliding speed characterized by the flow parameter λ. The dependence on sliding speed dominates in comparison with the dependence on the permeability. It is to be noted that the drag force is an average quantity over the entire particle surface, while permeability dependence is most significant at closest point of the surface to the wall (see e.g. Fig 2). The dependence on the permeability is nonetheless obvious by lower limit of λ that is set by the sticking point λ_s, i.e. $\lambda_s(\bar{\kappa}) < \lambda$. Similar to Fig. 9, plotting the drag force against the difference in flow parameter from the sticking point, $\lambda - \lambda_s$, the data collapse on a universal curve that follows $(\lambda - \lambda_s)^{-0.50}$ at low speeds and deviates from it at high speeds, $(\lambda - \lambda_s)^{-0.25}$, as shown in Fig. 11b. By fitting the data in Fig. 11a using power-law fits of type $F_D = a\lambda^{-0.5} + b\,(l_d h_0/R)^2 \ln(l_d h_0/R)^2$, where l_d is the domain size, and a and b are the fitting parameters, it is found that the leading order term governing the drag force scales as $a(\bar{\kappa})\lambda^{-0.50}$. The fitting parameter a is found to be independent of the domain size and the flow parameter, but dependent on the permeability. The value of a for impermeable particles is $a|_{\bar{\kappa}=0} = 0.54$, while for permeable particles $a|_{\bar{\kappa}\neq 0} / a|_{\bar{\kappa}=0} = \{1.89, 2.27, 2.52, 2.55\}$ for $\bar{\kappa} = \{0.207, 1.03, 2.07, 4.13\} \times 10^{-3}$, respectively.

5 Discussion and concluding remarks

In this work, we present a model of permeable particle sliding against a smooth rigid wall. The particle is pressed against the wall by the effect of the bulk system density. The model captures the flow details in the lubricated gap between the particle and the wall, and through the particle pores. The gap fluid and particle are coupled by the fluid pressure in the gap, the particle deformation, and the normal fluid velocity at the surface of the particle closest to the wall. Using this model, we study the behavior of particles with different permeability sliding at different speeds against a smooth rigid wall.

A pressure gradient develops in the lubricated layer between the wall and a deformable particle sliding against it, for both impermeable and permeable particles. A negative pressure develops at the particle rear which draws fluid to the gap and fluid is expelled from the gap in front of the particle, where positive pressure is developed. This pressure gradients serves to maintain the

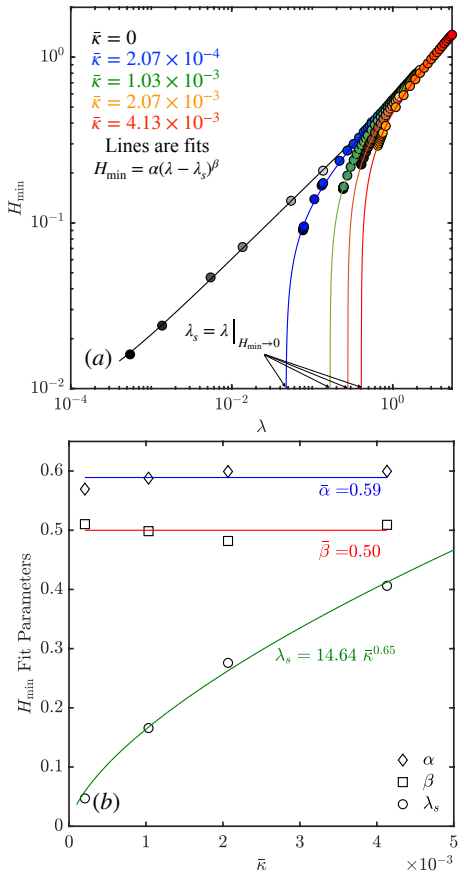

Fig. 8 Effect of particle permeability, $\bar{\kappa}$, on the minimum gap height, $H_{\min}$. (a) Minimum gap height along the sliding direction, i.e. $X-$axis of impermeable and permeable particles with different permeability values as a function of flow parameter λ. Lines are power-law fits of type $H_{\min} = \alpha(\lambda - \lambda_s)^{\beta}$. (b) Minimum gap height fitting parameter. The pre-factor α and exponent β are almost identical for all permeability values and their average values are $\bar{\alpha} = 0.59$, and $\bar{\beta} = 0.50$. The dependence of the flow parameter on the permeability follows the power law, $\bar{\lambda}_s = 14.64\bar{\kappa}^{0.65}$.

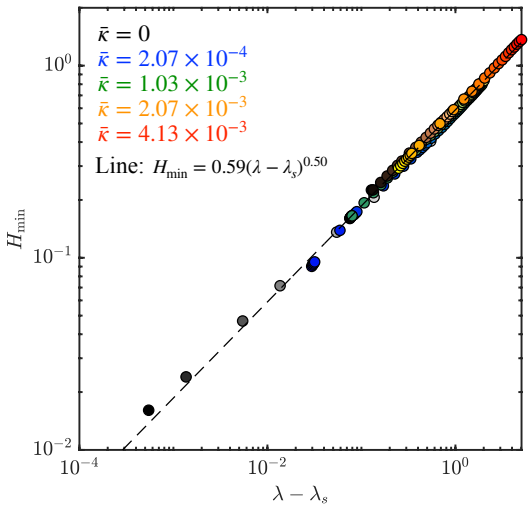

Fig. 9 Minimum gap height along the sliding direction, i.e. $X-$axis of impermeable and permeable particles with different permeability values plotted against the difference between the flow parameter and the sticking point, $\lambda - \lambda_s$. Dashed line is a power law fit using the average values of the fitting parameters in Fig. 8b.

lubricated layer. A permeable particle are found to approach the wall more than an impermeable particle sliding near the wall at the same speed. The fluid pressure in the gap is lower in magnitude than the pressure developed in the case of impermeable particles. This pressure reduction is primarily due to the excess fluid flow from and to the particle pores at the negative and positive pressure region, respectively.

The flow through the particle pores underlies the difference in slip behavior between permeable and impermeable particles sliding near a wall and it is regulated by the permeability. The effect of permeability can be summarized as follows. The net flow to the particle is found to increase with increasing permeability. At a certain permeability, the minimum gap height decreases with decreasing permeability until a critical point λ_s – the sticking point – where the particle first makes contact with the wall. This sticking point is found to increase with increasing permeability as $\lambda_s \sim \bar{\kappa}^{0.65}$. The pressure developed in the lubricated layer result in a drag force on the particle. The drag force is dominated by the sliding speed. However, the sliding speed itself is implicitly dependent on the permeability via the dependence of the sticking point on the permeability. This results reveal the strong coupling between the fluid dynamics in the gap and the fluid flow through the permeable particle. All of these results and the fact that permeable particles tend to get closer to the wall than their impermeable counterparts sliding at the same speed, and that impermeable-particle systems can slip with much lower speeds without sticking, confirm that permeable particles are *sticky*.

The sticky behavior of permeable particle is similar to the behavior observed in[35], of impermeable particle with short-range attraction with the wall. Wall slip is known to depend on the smooth-surface chemistry[12,35,56,57]. Typical gap height values are on the order of $2-10$ nm[11,28,35], in the range wall-particle interactions can be important. Short-range attractive forces originate from attractive van der Waals forces, and/or the hydrophobic nature of the surface, which favors weak particle-surface attractions. In principle, one can predict the wall-slip behavior of permeable particles by constructing an attractive pressure acting across the film[12,35]. For example, the permeability can acts as an effective Hamaker constant in van der Waals pressure[35]. This procedure is efficient and effective in predicting the gap height and the general slip behavior, but fails to predict the flow details and its effect on the gap fluid pressure.

The flow of the gap fluid through the particle pores effectively suppresses wall-slip and instead sticking occurs at λ_s depending on the permeability. This result supports the recent findings that particle-scale features are necessary and sufficient to effectively predict wall slip in dense soft microgel suspensions[58]; here, we describe particle-scale features with the particle permeability. In fact, the permeability offers an alternative way to avoid wall-slip, in lieu of suppressing slip via the introduction of wall roughness. Former studies assert that slip is suppressed when surface asperity

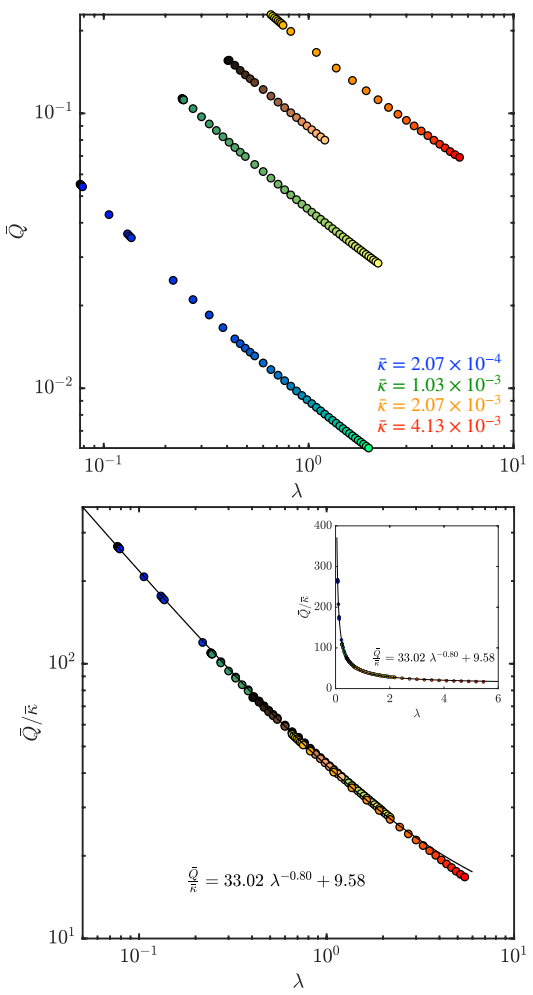

Fig. 10 Effect of particle permeability, $\bar{\kappa}$, on the net flow from the particle, $\bar{Q}$. (a) Net flow from particles of different permeability values. (b) Scaling the net flow by the dimensionless permeability results in a collapse of the data on a universal curve. The net flow scaled with permeability scales with the flow parameter as $\bar{Q}/\bar{\kappa} \sim \lambda^{-0.8}$. Inset in (b) shows the same data on linear axes.

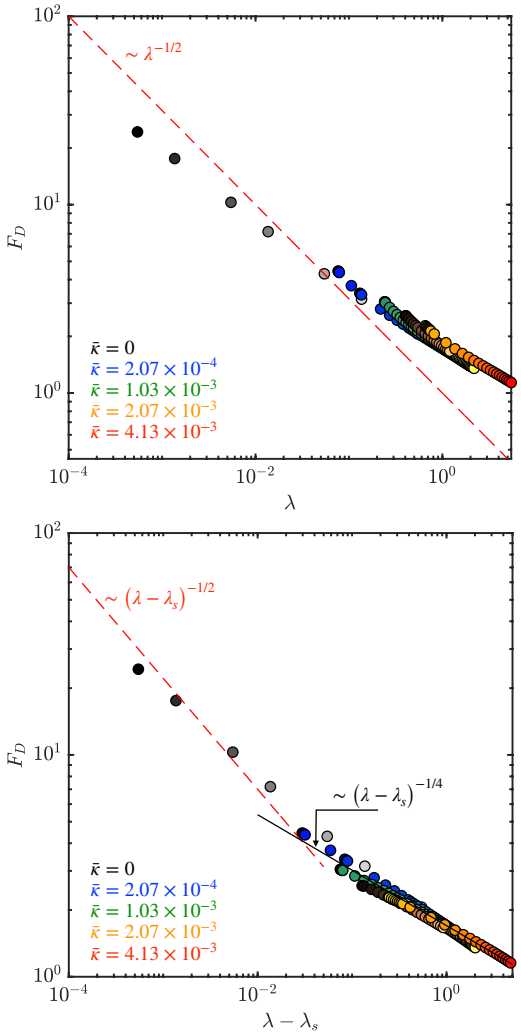

Fig. 11 Effect of particle permeability, $\bar{\kappa}$, on the drag force, F_D. (a) Drag force impermeable and permeable particles with different permeability values as a function of flow parameter λ. (b) Drag force plotted as a function of the difference of flow parameter and sticking point, $\lambda - \lambda_s$.

height R_a is of the same order as particle radius R, i.e. $R/R_a \leq 1$[32,59]. Let us assume the following; the suppression of slip in permeable particles to originate from particle-surface roughness instead of wall roughness. In this case, we can characterize the surface roughness of the particle in terms of its permeability; that is $R_a < \sqrt{\kappa}$. We estimate the particle radius-to-asperity ratio as $R/R_a > 10^2$. This observation confirms that slip can be suppressed at even much finer particle-surface features than the minimum required wall-surface features for slip suppression.

The model presented in this paper and the presented results offer ample opportunities to explore particle permeability to control slip-stick behavior and consequently bulk mechanical properties. The permeability of soft particles, such as microgels and star polymers, can be tuned by several external stimuli such as applied deformation[42,60–62], pH[63,64], temperature[63,65], or magnetic fields[66–68]. An area that is yet to be explored is using such external stimuli to trigger stick or slip behavior even at the same sliding speed.

Author Contributions

M. Z.: Methodology, Software, Investigation, Formal Analysis, Validation, Visualization, Data Curation, Writing - Original Draft. **R. B.:** Conceptualization, Methodology, Resources, Supervision, Funding Acquisition, Writing - Review & Editing.

Conflicts of interest

There are no conflicts to declare.

Acknowledgements

We gratefully acknowledge partial financial support from the National Science Foundation (MRSEC under Award No. DMR-1720595).

Notes and references

1 C. W. A. Bromley, *J. Coat. Technol.*, 1989, **61**, 39–43.
2 N. L. Thomas, *Prog. Org. Coat.*, 1991, **19**, 101–121.

3 D. Saatweber and B. Vogt-Birnbrich, *Prog. Org. Coat.*, 1996, **28**, 33–41.
4 J. D. Smart, *Adv. Drug Deliv. Rev.*, 2005, **57**, 1556–1568.
5 Q. Wang, Y. Zhao, Y. Yang, H. Xu and X. Yang, *Colloid Polym. Sci.*, 2007, **285**, 515–521.
6 J. R. Stokes and W. J. Frith, *Soft Matter*, 2008, **4**, 1133–1140.
7 P. Burey, B. R. Bhandari, T. Howes and M. J. Gidley, *Crit. Rev. Food Sci. Nutr.*, 2008, **48**, 361–377.
8 A. Bouchoux, P.-E. Cayemitte, J. Jardin, G. Gésan-Guiziou and B. Cabane, *Biophys. J.*, 2009, **96**, 693–706.
9 C. B. Highley, K. H. Song, A. C. Daly and J. A. Burdick, *Adv. Sci.*, 2019, **6**, 1801076.
10 H. A. Barnes, *J. Non-Newtonian Fluid Mech.*, 1995, **56**, 221–251.
11 S. P. Meeker, R. T. Bonnecaze and M. Cloitre, *Journal of Rheology*, 2004, **48**, 1295–1320.
12 M. Cloitre and R. T. Bonnecaze, *Rheol. Acta*, 2017, **56**, 283–305.
13 S. G. Hatzikiriakos and K. B. Migler, *Polymer processing instabilities: Control and understanding*, CRC Press, 2004.
14 T. F. Ballenger, I.-J. Chen, J. W. Crowder, G. E. Hagler, D. C. Bogue and J. L. White, *Trans. Soc. Rheol.*, 1971, **15**, 195–215.
15 P. Beaufils, B. Vergnes and J. F. Agassant, *Int. Polym. Proc.*, 1989, **4**, 78–84.
16 J. Molenaar and R. J. Koopmans, *J. Rheol.*, 1994, **38**, 99–109.
17 J. R. Stokes, M. W. Boehm and S. K. Baier, *Curr. Opin. Colloid Interface Sc.*, 2013, **18**, 349–359.
18 S. Roman, A. Merlo, P. Duru, F. Risso and S. Lorthois, *Biomicrofluidics*, 2016, **10**, 034103.
19 K. Wolff, D. Marenduzzo and M. E. Cates, *J. R. Soc. Interface*, 2012, **9**, 1398–1408.
20 S. K. Lai, Y.-Y. Wang, D. Wirtz and J. Hanes, *Adv. Drug Deliv. Rev.*, 2009, **61**, 86–100.
21 E. Lauga, M. Brenner and H. Stone, *Springer Handbooks*, Springer, 2007, pp. 1219–1240.
22 T. Lee, E. Charrault and C. Neto, *Adv. Colloid Interface Sci.*, 2014, **210**, 21–38.
23 H. Tabuteau, J.-C. Baudez, F. Bertrand and P. Coussot, *Rheol. Acta*, 2004, **43**, 168–174.
24 D. D. Joseph, *Powder Technol.*, 1997, **94**, 211–215.
25 P. Morell, I. Hernando and S. M. Fiszman, *Trends Food Sci. Technol*, 2014, **35**, 18–31.
26 J. Chen, Z. Liu and S. Prakash, *Food Hydrocoll.*, 2014, **42**, 100–105.
27 S. A. Khan, C. A. Schnepper and R. C. Armstrong, *J. Rheol.*, 1988, **32**, 69–92.
28 S. P. Meeker, R. T. Bonnecaze and M. Cloitre, *Physical Review Letters*, 2004, **92**, 198302.
29 A. Magnin and J. M. Piau, *J. Non-Newtonian Fluid Mech.*, 1990, **36**, 85–108.
30 S. A. Gulmus and U. Yilmazer, *J. Appl. Polym.*, 2005, **98**, 439–448.
31 C. S. Nickerson and J. A. Kornfield, *J. Rheol.*, 2005, **49**, 865–874.
32 B. K. Aral and D. M. Kalyon, *J. Rheol.*, 1994, **38**, 957–972.
33 G. H. Meeten, *Rheol. Acta*, 2004, **43**, 6–16.
34 R. N. Zia, B. Landrum and W. B. Russel, *J. Rheol.*, 2014, **58**, 1121–1157.
35 J. R. Seth, M. Cloitre and R. T. Bonnecaze, *Journal of Rheology*, 2008, **52**, 1241–1268.
36 J. R. Seth, C. Locatelli-Champagne, F. Monti, R. T. Bonnecaze and M. Cloitre, *Soft Matter*, 2012, **8**, 140–148.
37 M. Jalaal, N. J. Balmforth and B. Stoeber, *Langmuir*, 2015, **31**, 12071–12075.
38 C.-Y. Hui, Z. Liu, N. Bain, A. Jagota, E. R. Dufresne, R. W. Style, R. Kiyama and J. P. Gong, *Proc. R. Soc. A*, 2020, **476**, 20200477.
39 D. Vlassopoulos and M. Cloitre, *Curr. Opin. Colloid Interface Sc.*, 2014, **19**, 561–574.
40 R. T. Bonnecaze and M. Cloitre, *Adv. Polym. Sci.*, 2010, 117–161.
41 M. E. A. Zakhari, P. D. Anderson and M. Hütter, *Phys. Rev. E*, 2017, **96**, 012604.
42 M. E. A. Zakhari, M. Hütter and P. D. Anderson, *J. Rheol.*, 2018, **62**, 543–557.
43 L. G. Leal, *Advanced transport phenomena: Fluid mechanics and convective transport processes*, Cambridge University Press, 2007, vol. 7.
44 K. L. Johnson, *Contact mechanics*, Cambridge university press, 1985.
45 J. Bear, *Dynamics of fluids in porous media*, Dover, 2013.
46 R. H. Davis, J.-M. Serayssol and E. J. Hinch, *J. Fluid Mech.*, 1986, **163**, 479–497.
47 W. L. Bargar and J. L. Nowinski, *Acta Mech.*, 1974, **20**, 217–231.
48 A. Verruijt, *An introduction to soil dynamics*, Springer Science & Business Media, 2009, vol. 24.
49 W. S. Hall, *The boundary element method*, Springer, 1994, pp. 61–83.
50 K.-C. Ang, *Int. J. Math. Educ. Sci. Technol.*, 2008, **39**, 505–519.
51 P. K. Kythe, *An introduction to boundary element methods*, CRC press, 2020.
52 M. E. O'Neill and K. Stewartson, *J. Fluid Mech.*, 1967, **27**, 705–724.
53 T. G. Mason, M.-D. Lacasse, G. S. Grest, D. Levine, J. Bibette and D. A. Weitz, *Phys. Rev. E*, 1997, **56**, 3150.
54 C. A. Grattoni, H. H. Al-Sharji, C. Yang, A. H. Muggeridge and R. W. Zimmerman, *J. Colloid Interface Sci.*, 2001, **240**, 601–607.
55 H. Wu, N. Moyle, A. Jagota and C.-Y. Hui, *Soft Matter*, 2020, **16**, 2760–2773.
56 S. G. Hatzikiriakos and J. M. Dealy, *Int. Polym. Process.*, 1993, **8**, 36–43.
57 H. J. Walls, S. B. Caines, A. M. Sanchez and S. A. Khan, *J. Rheol.*, 2003, **47**, 847–868.
58 J. Péméja, B. Géraud, C. Barentin and M. Le Merrer, *Phys. Rev. Fluids*, 2019, **4**, 033301.

59 S. A. Gulmus and U. Yilmazer, *J. Appl. Polym. Sci.*, 2007, **103**, 3341–3347.
60 J. R. Stokes, *Microgel Suspensions: Fundamentals and Applications*, Wiley Online Library, 2011, pp. 327–353.
61 T. Kawasaki, A. Ikeda and L. Berthier, *EPL*, 2014, **107**, 28009.
62 A. Le Grand and G. Petekidis, *Rheol. Acta*, 2008, **47**, 579–590.
63 T. Hoare and R. Pelton, *Macromolecules*, 2004, **37**, 2544–2550.
64 D. Dupin, J. Rosselgong, S. P. Armes and A. F. Routh, *Langmuir*, 2007, **23**, 4035–4041.
65 H. Senff and W. Richtering, *J. Chem. Phys.*, 1999, **111**, 1705–1711.
66 J. E. Wong, A. K. Gaharwar, D. Müller-Schulte, D. Bahadur and W. Richtering, *J. Magn. Magn. Mater.*, 2007, **311**, 219–223.
67 J. E. Wong, A. K. Gaharwar, D. Müller-Schulte, D. Bahadur and W. Richtering, *J. Colloid Interface Sci.*, 2008, **324**, 47–54.
68 C. Dagallier, H. Dietsch, P. Schurtenberger and F. Scheffold, *Soft Matter*, 2010, **6**, 2174–2177.